

# Propagative Block Diagonalisation Diabatisation of DFT/MRCI Electronic States

Simon P. Neville,<sup>1,\*</sup> Issaka Seidu,<sup>1</sup> and Michael S. Schuurman<sup>1,2</sup>

<sup>1</sup>*Department of Chemistry and Biomolecular Sciences, University of Ottawa,  
10 Marie Curie, Ottawa, Ontario, K1N 6N5, Canada*

<sup>2</sup>*National Research Council of Canada, 100 Sussex Drive, Ottawa, Ontario K1A 0R6, Canada*

We present a framework for the calculation of diabatic states using the combined density functional theory and multireference configuration interaction (DFT/MRCI) method. Due to restrictions present in the current formulation of the DFT/MRCI method (a lack of analytical derivative couplings and the inability to use non-canonical Kohn-Sham orbitals), most common diabatisation strategies are not applicable. We demonstrate, however, that diabatic wavefunctions and potentials can be calculated at the DFT/MRCI level of theory using a propagative variant of the block diagonalisation diabatisation method (P-BDD). The proposed procedure is validated *via* the calculation of diabatic potentials for LiH and the simulation of the vibronic spectrum of pyrazine. In both cases, the combination of the DFT/MRCI and P-BDD methods is found to correctly recover the non-adiabatic coupling effects of the problem.

## I. INTRODUCTION

Since its introduction by Grimme and Waletzke[1], the combined density functional theory and multireference configuration interaction (DFT/MRCI) method has proved to be a uniquely powerful general purpose semi-empirical method for the calculation of the excited states of large molecules. Advantages of the DFT/MRCI method include its accuracy, computational efficiency, black box nature, and its ability to correctly describe a wide range of classes of excited states, including those of valence, Rydberg, charge transfer, and doubly-excited character. Although originally conceived as a method for the description of singlet and triplet states in organic molecules, recent developments by Marian and co-workers have resulted in a spin multiplicity-independent redesign of the DFT/MRCI Hamiltonian[2, 3], and a reparameterisation for an improved description of transition metal complexes[4].

The DFT/MRCI method has seen extensive use in the characterization of excited state surfaces including the calculation of excitation energies, spin-orbit couplings and photochemical reaction pathways[5–10]. One area where DFT/MRCI has seen less use, however, is in conjunction with time-dependent quantum dynamics calculations. The starting point for such studies is the extraction of potential energy surfaces and non-adiabatic couplings in a suitable form. This may either be in the adiabatic representation, where the couplings between the electronic states are described by derivative coupling matrix elements, or in a diabatic representation, in which the interstate couplings are described by off-diagonal elements of the potential matrix. Due to singularities present in the derivative coupling terms in the adiabatic representation, it is often preferable to turn to a

diabatic representation, where they are eliminated. Furthermore, analytic derivative couplings are not available at the DFT/MRCI level of theory. Thus, one is naturally prompted to explore methods for the calculation of diabatic potential matrices using DFT/MRCI.

For polyatomic molecules, the generation of strictly diabatic states (which exactly remove the derivative couplings) is not possible[11]. Instead, one seeks a set of so-called quasi-diabatic states that minimise the derivative coupling terms, or at least remove the singular components of them. There is no unique solution to this problem, and, accordingly, a large number of diabatisation schemes have been developed over the years. For an overview of some of representative examples, we direct the reader to References 12–23. However, many of the existing methods are not compatible with the current formulation of DFT/MRCI. The reasons for this are twofold. Firstly, the inability to compute analytic derivative couplings means that all of the methods employing them[15, 16, 20, 22, 23] cannot be leveraged. Secondly, DFT/MRCI requires the use of the canonical Kohn-Sham (KS) orbitals as the single-particle basis, rendering it incompatible with any method that uses bases of diabatic molecular orbitals (MOs)[12–14, 19]. In fact, beyond property-based diabatisation methods[21] and strategies based on diabatisation by *ansatz* (involving the fitting of pre-specified functional forms to adiabatic energies), we are not aware of any currently implemented diabatisation schemes that are suitable for use with DFT/MRCI.

To proceed to a solution to this problem, we re-visit the block diagonalisation diabatisation (BDD) method of Pacher, Cederbaum and Köppel[17, 18, 24]. The BDD method requires only wavefunction information, making it compatible with DFT/MRCI. Previous *ab initio* implementations of this method have, however, been based around the construction of configuration state functions (CSFs) in a diabatic MO basis[25–29], which is not possible with DFT/MRCI. Instead, we consider an idea explored by Pacher, Cederbaum and Köppel many years ago[18], but never before implemented in an *ab initio* study. Specifically, we implement a propagative BDD

---

\*Electronic address: simon.neville@nrc-cnrc.gc.ca; Current Address: National Research Council of Canada, 100 Sussex Drive, Ottawa, Ontario K1A 0R6, Canada

(P-BDD) algorithm that requires only the overlaps of adiabatic electronic wavefunctions at neighboring nuclear geometries. In this implementation, the BDD method is directly compatible with DFT/MRCI.

The rest of this paper is organised as follows. In Section II, we give a discussion of the P-BDD algorithm and the details of an efficient wavefunction overlap scheme that renders it computationally tractable. In Section IV, we assess the quality of the diabatic potentials yielded by the combination of DFT/MRCI and P-BDD methods. Firstly, the diabatic potentials of the first two  $^1\Sigma^+$  states of LiH were calculated and compared to the results of canonical MRCI computations. Secondly, a model vibronic coupling Hamiltonian for pyrazine was parameterised using the results of DFT/MRCI P-BDD calculations and used in the simulation of its absorption spectrum. In the case of LiH, the DFT/MRCI P-BDD diabatic potentials were found to yield derivative couplings in good agreement with the canonical MRCI results. For pyrazine, the simulated absorption spectrum was found to be in excellent agreement with its experimental counterpart. Through these results, we conclude that the combination of the DFT/MRCI and P-BDD methods offers a reliable, near-black box route to the calculation of diabatic potentials.

## II. THEORETICAL FRAMEWORK

### A. Propagative block diagonalisation diabatisation

We begin with the introduction of some notation. In the following,  $\mathbf{r}$  and  $\mathbf{R}$  are used to denote the vectors of electronic and nuclear coordinates, respectively. Let  $\hat{H}$  denote the total molecular Hamiltonian, partitioned as

$$\hat{H}(\mathbf{r}, \mathbf{R}) = \hat{T}_n(\mathbf{R}) + \hat{H}_{el}(\mathbf{r}, \mathbf{R}), \quad (1)$$

where  $\hat{T}_n(\mathbf{R})$  is the nuclear kinetic energy operator and  $\hat{H}_{el}(\mathbf{r}, \mathbf{R})$  the electronic Hamiltonian, that is, the sum of the electronic and nuclear kinetic energy operator and all Coulombic potential terms. The set of eigenfunctions of  $\hat{H}_{el}(\mathbf{r}, \mathbf{R})$  (the set of adiabatic electronic states) is denoted by  $\{\psi_I(\mathbf{r}; \mathbf{R})\}$ . The corresponding eigenvalues (the adiabatic potentials) are denoted by  $V_I(\mathbf{R})$ . Our goal is to compute a set  $\{\phi_I(\mathbf{r}; \mathbf{R})\}$  of quasi-diabatic states, related to the adiabatic states through the adiabatic-to-diabatic transformation (ADT) matrix  $\mathbf{U}(\mathbf{R})$ :

$$\phi_I(\mathbf{r}; \mathbf{R}) = \sum_J U_{JI}(\mathbf{R}) \psi_J(\mathbf{r}; \mathbf{R}). \quad (2)$$

Finally, let  $\{\Phi_I(\mathbf{r}; \mathbf{R})\}$  be a set of ‘initial’, or ‘reference’, states in terms of which the Hamiltonian is to be initially represented. More will subsequently be said about the possible choices for the initial states, but for now they are left unspecified beyond being taken to form a complete

orthonormal basis in which the molecular wavefunction can be represented.

A key idea underlying the BDD method is that, within the framework of the group Born-Oppenheimer approximation, it is usually possible to identify a finite subset  $P$  of states of interest that are well separated from, and only weakly coupled to, their orthogonal complement of states, termed the  $Q$  space states. We may then seek an ADT matrix  $\mathbf{U}(\mathbf{R})$  that operates only in the  $P$  space of states, i.e., with the structure

$$\mathbf{U}(\mathbf{R}) = \begin{pmatrix} \mathbf{U}_P(\mathbf{R}) & \mathbf{0} \\ \mathbf{0} & \mathbf{1} \end{pmatrix}, \quad (3)$$

where  $\mathbf{U}_P(\mathbf{R})$  denotes the  $P$  space part of  $\mathbf{U}(\mathbf{R})$ . It is obvious that any such  $P$  space transformation will result in a representation of the electronic Hamiltonian that is block diagonal in the  $P$  and  $Q$  spaces. Knowing that a quasi-diabatisation within the  $P$  space will yield a block diagonal electronic Hamiltonian, a natural question to ask is whether we can determine a block diagonalisation transformation of the electronic Hamiltonian matrix that leads to quasi-diabatic states? This is exactly the issue addressed by Pacher, Cederbaum and Köppel in their BDD scheme[17, 18, 24].

The electronic Hamiltonian is first represented using the basis  $\{\Phi_I(\mathbf{r}; \mathbf{R})\}$  of initial states:

$$H_{IJ}(\mathbf{R}) = \left\langle \Phi_I(\mathbf{r}; \mathbf{R}) \left| \hat{H}_{el} \right| \Phi_J(\mathbf{r}; \mathbf{R}) \right\rangle. \quad (4)$$

A unitary transformation  $\mathbf{B}(\mathbf{R})$  is sought that brings the initial state electronic Hamiltonian matrix  $\mathbf{H}(\mathbf{R})$  into the desired block diagonal form, denoted by  $\mathcal{H}(\mathbf{R})$ :

$$\begin{aligned} \mathcal{H}(\mathbf{R}) &= \mathbf{B}^\dagger(\mathbf{R}) \mathbf{H}(\mathbf{R}) \mathbf{B}(\mathbf{R}) \\ &= \begin{pmatrix} \mathcal{H}_P & \mathbf{0} \\ \mathbf{0} & \mathcal{H}_Q \end{pmatrix}. \end{aligned} \quad (5)$$

There are an infinite number of transformations  $\mathbf{B}(\mathbf{R})$  that will result in the desired block diagonal structure, and a constraint must be introduced. In particular, in the BDD scheme, the constraint used takes the form of a ‘least action principle’ of the form

$$\|\mathbf{B}(\mathbf{R}) - \mathbf{1}\| = \min, \quad (6)$$

where  $\|\cdot\|$  denotes the Frobenius norm. That is, the transformation  $\mathbf{B}(\mathbf{R})$  is constrained to block diagonalise the initial state electronic Hamiltonian matrix  $\mathbf{H}(\mathbf{R})$ , but beyond that do as little as possible. With this one constraint in place, the transformation  $\mathbf{B}(\mathbf{R})$  may be uniquely determined to take the following form[17, 30]:

$$\mathbf{B}(\mathbf{R}) = \mathbf{Z}(\mathbf{R}) \left( \mathbf{Z}^\dagger(\mathbf{R}) \mathbf{Z}(\mathbf{R}) \right)^{-\frac{1}{2}}, \quad (7)$$

where

$$\mathbf{Z}(\mathbf{R}) = \mathbf{S}(\mathbf{R})\mathbf{S}_{BD}^{-1}(\mathbf{R}). \quad (8)$$

Here,  $\mathbf{S}(\mathbf{R})$  denotes the matrix over overlaps between the initial and adiabatic electronic states,

$$S_{IJ}(\mathbf{R}) = \langle \Phi_I(\mathbf{r}; \mathbf{R}) | \psi_J(\mathbf{r}; \mathbf{R}) \rangle, \quad (9)$$

and  $\mathbf{S}_{BD}(\mathbf{R})$  is its block diagonal part:

$$\mathbf{S}_{BD}(\mathbf{R}) = \begin{pmatrix} \mathbf{S}_P(\mathbf{R}) & \mathbf{0} \\ \mathbf{0} & \mathbf{S}_Q(\mathbf{R}) \end{pmatrix}. \quad (10)$$

Finally, by making use of the relation

$$\mathbf{B}(\mathbf{R}) = \mathbf{S}(\mathbf{R})\mathbf{U}(\mathbf{R}), \quad (11)$$

the ADT matrix  $\mathbf{U}(\mathbf{R})$  may be written as

$$\mathbf{U}(\mathbf{R}) = \mathbf{S}_{BD}^{-1}(\mathbf{R})(\mathbf{S}_{BD}(\mathbf{R})\mathbf{S}_{BD}^\dagger(\mathbf{R}))^{\frac{1}{2}}. \quad (12)$$

Importantly, the  $P$  space part of  $\mathbf{U}(\mathbf{R})$  that we require can be computed using only the  $P$  space part of  $\mathbf{S}_{BD}(\mathbf{R})$ . That is, using only the overlaps of the initial and adiabatic electronic states spanning the  $P$  space:

$$\mathbf{U}_P(\mathbf{R}) = \mathbf{S}_P^{-1}(\mathbf{R})(\mathbf{S}_P(\mathbf{R})\mathbf{S}_P^\dagger(\mathbf{R}))^{\frac{1}{2}}. \quad (13)$$

All we then require is a prescription for the choice of the initial states  $\Phi_I(\mathbf{r}; \mathbf{R})$ .

In order for the transformation  $\mathbf{B}(\mathbf{R})$  to rotate the initial basis into a good set of quasi-diabatic states  $\{\phi_I(\mathbf{r}; \mathbf{R})\}$ , it is required that the initial states  $\Phi_I(\mathbf{r}; \mathbf{R})$  themselves already behave somewhat quasi-diabatically, or at least vary smoothly with the nuclear geometry, as can be deduced from the least action principle, Equation 6. Soon after the development of the BDD method, it was recognised that a convenient choice of such a set of initial states is the set of CSFs used to expand the adiabatic states represented in terms of diabatic MOs[25, 26]. That is, MOs obtained from the canonical set by a unitary transformation to maximise their overlap with the canonical MOs at some reference geometry  $\mathbf{R}_0$ . In practical *ab initio* calculations, this turns out to be an excellent choice as  $\mathbf{S}_P(\mathbf{R})$  then reduces to the matrix of expansion coefficients for the electronic states in the basis of the CSFs formed from the diabatic MOs. Indeed, this approach has proved to be very successful, and implementations have been reported at the complete active space self consistent field (CASSCF)[25–27], multi-reference configuration interaction (MRCI)[28] and equation-of-motion coupled cluster (EOM-CC)[29] levels of theory.

However, the use of diabatic CSFs as the initial states is not compatible with DFT/MRCI, which requires the

use of the canonical KS orbitals. Instead, we re-visit a suggestion first put forwards by Pacher, Cederbaum and Köppel in Reference 18, but, as far as we are aware, never implemented beyond model studies. The idea is to generate an initial basis  $\{\Phi_I(\mathbf{r}; \mathbf{R})\}$  in a propagative manner. Firstly, a reference geometry  $\mathbf{R}_0$  is defined, at which the adiabatic and diabatic representations are taken to be equal, fixing the global gauge of the adiabatic-to-diabatic transformation. Next, a string of displaced geometries  $\mathbf{R}_n = \mathbf{R}_0 + n\Delta\mathbf{R}$  is chosen, at which the ADT matrix is to be calculated. At the first geometry,  $\mathbf{R}_1$ , the adiabatic states  $\{\psi_I(\mathbf{r}; \mathbf{R}_0)\}$  of the reference geometry are used as the initial states. That is,  $\{\Phi_I(\mathbf{r}; \mathbf{R}_1)\} = \{\psi_I(\mathbf{r}; \mathbf{R}_0)\}$ . This is equivalent to using a crude adiabatic basis as the initial states at  $\mathbf{R}_1$ . The overlaps between the sets of states  $\{\psi_I(\mathbf{r}; \mathbf{R}_0)\}$  and  $\{\psi_I(\mathbf{r}; \mathbf{R}_1)\}$  are calculated, and used in the construction of the  $P$  space ADT matrix  $\mathbf{U}_P(\mathbf{R}_1)$ , as given in Equation 13. At the next geometry,  $\mathbf{R}_2$ , the quasi-diabatic states  $\{\phi_I(\mathbf{r}; \mathbf{R}_1)\}$  from  $\mathbf{R}_1$ , calculated using  $\mathbf{U}_P(\mathbf{R}_1)$ , are used as the initial states, yielding the ADT matrix  $\mathbf{U}_P(\mathbf{R}_2)$ . This process is repeated, using the quasi-diabatic states from the geometry  $\mathbf{R}_n$  as the initial states for the geometry  $\mathbf{R}_{n+1}$ .

The above described propagative BDD, or P-BDD, scheme leads to an optimal set of quasi-diabatic states  $\{\phi_I(\mathbf{r}; \mathbf{R})\}$  in the limit of infinitesimal displacements  $\Delta\mathbf{R}$ . Here, the term optimal is used in the sense of minimising the integral of the squared norm of the  $P$  space derivative coupling matrix over the path connecting the nuclear coordinates  $\mathbf{R}_0, \mathbf{R}_1, \dots, \mathbf{R}_n$  (see Reference 18 for details). However, the P-BDD method has not yet seen use beyond the solution of model diabatisation problems[18]. This seems to be rooted in the potential difficulties associated with the efficient calculation of overlaps of electronic wavefunctions computed at different nuclear geometries, i.e., using non-orthogonal sets of MOs. In Section II B, we describe our approach to dealing with this problem.

## B. Efficient calculation of wavefunction overlaps

In order to calculate the ADT matrix of the P-BDD scheme, we have to compute the overlap matrix elements

$$\begin{aligned} S_{IJ}(\mathbf{R}_{n+1}) &= \langle \phi_I(\mathbf{r}; \mathbf{R}_n) | \psi_J(\mathbf{r}; \mathbf{R}_{n+1}) \rangle \\ &= \sum_K U_{IK}^\dagger(\mathbf{R}_n) \langle \psi_K(\mathbf{r}; \mathbf{R}_n) | \psi_J(\mathbf{r}; \mathbf{R}_{n+1}) \rangle. \end{aligned} \quad (14)$$

That is, only the overlaps between adiabatic electronic states at neighboring geometries are needed as input. This is compatible with the DFT/MRCI method. However, the success of this scheme relies on the ability to rapidly compute overlaps between wavefunctions expressed in terms of non-orthogonal orbitals. Careful attention has to be paid here as, if naively implemented, this can be disastrously slow for large wavefunction ex-

pansions. Our strategy here is based on a modification of the algorithm originally presented by Plasser *et al.*[31].

We consider the calculation of the set  $\{\langle\psi_I|\psi'_J\rangle\}$  of all possible overlaps between two sets of electronic states  $\{\psi_I\}$  and  $\{\psi'_J\}$ . Here, we drop the explicit labeling of the coordinate dependence of the electronic states to avoid unwieldy expressions. In the context of a P-BDD calculation, the two sets of states would be the adiabatic electronic states at two neighboring geometries. The states in the sets  $\{\psi_I\}$  and  $\{\psi'_J\}$  are in turn expanded in terms of sets of Slater determinants  $\{\Theta_k\}$  and  $\{\Theta'_k\}$ :

$$\psi_I = \sum_{k=1}^{N_I} C_{kI} \Theta_k, \quad (15)$$

$$\psi'_I = \sum_{k=1}^{N'_I} C'_{kI} \Theta'_k. \quad (16)$$

Finally, the Slater determinants are expressed in terms of sets of spin orbitals  $\{\varphi_n, \bar{\varphi}_n\}$  and  $\{\varphi'_n, \bar{\varphi}'_n\}$ :

$$\Theta_k = \left| \varphi_{i_1^k} \cdots \varphi_{i_{n_\alpha}^k} \bar{\varphi}_{i_1^k} \cdots \bar{\varphi}_{i_{n_\beta}^k} \right|, \quad (17)$$

---


$$\langle \Theta_k | \Theta'_l \rangle = \begin{vmatrix} \langle \varphi_{i_1^k} | \varphi'_{i_1^l} \rangle & \cdots & \langle \varphi_{i_{n_\alpha}^k} | \varphi'_{i_{n_\alpha}^l} \rangle & & & \\ \vdots & \ddots & \vdots & & & \\ \langle \varphi_{i_{n_\alpha}^k} | \varphi'_{i_1^l} \rangle & \cdots & \langle \varphi_{i_{n_\alpha}^k} | \varphi'_{i_{n_\alpha}^l} \rangle & & & \\ & & \mathbf{0} & & & \\ & & & \langle \bar{\varphi}_{i_1^k} | \bar{\varphi}'_{i_1^l} \rangle & \cdots & \langle \bar{\varphi}_{i_1^k} | \bar{\varphi}'_{i_{n_\beta}^l} \rangle \\ & & & \vdots & \ddots & \vdots \\ & & & \langle \bar{\varphi}_{i_{n_\beta}^k} | \bar{\varphi}'_{i_1^l} \rangle & \cdots & \langle \bar{\varphi}_{i_{n_\beta}^k} | \bar{\varphi}'_{i_{n_\beta}^l} \rangle \end{vmatrix} = \begin{vmatrix} \mathbf{s}_{kl} & \mathbf{0} \\ \mathbf{0} & \bar{\mathbf{s}}_{kl} \end{vmatrix} = \det(\mathbf{s}_{kl}) \times \det(\bar{\mathbf{s}}_{kl}) \quad (20)$$


---

If directly implemented, with the calculation of the factors  $\det(\mathbf{s}_{kl})$  and  $\det(\bar{\mathbf{s}}_{kl})$  being performed on-the-fly for every pair of Slater determinants, the computational effort for the calculation of the wavefunction overlap  $\langle\psi_I|\psi_J\rangle$  scales as  $N_I N'_J n_{el}^3$ , where  $N_I$  and  $N'_J$  are the number of Slater determinants in the expansion of  $\psi_I$  and  $\psi'_J$ , respectively, and  $n_{el}$  is the number of electrons. For DFT/MRCI wavefunctions, the dimension of the Slater determinant basis is usually  $\mathcal{O}(10^4 - 10^6)$ , resulting in potentially ruinous computational costs.

A way to alleviate this bottleneck was recently put forward by Plasser *et al.*[31]. As the authors noted, the factors  $\det(\mathbf{s}_{kl})$  and  $\det(\bar{\mathbf{s}}_{kl})$  are not unique to the pair of Slater determinants  $\Theta_k$  and  $\Theta'_l$ , but also occur for other Slater determinants with the same  $\alpha$  and  $\beta$  spin orbital occupations. By precomputing and storing all unique factors for the wavefunction pair  $\psi_I$  and  $\psi'_J$ , speedups of

$$\Theta'_k = \left| \varphi'_{i_1^k} \cdots \varphi'_{i_{n_\alpha}^k} \bar{\varphi}'_{i_1^k} \cdots \bar{\varphi}'_{i_{n_\beta}^k} \right|. \quad (18)$$

Here,  $\varphi$  and  $\bar{\varphi}$  are used to denote  $\alpha$  and  $\beta$  spin orbitals, respectively, and  $n_\alpha$  and  $n_\beta$  the number of  $\alpha$  and  $\beta$  electrons. The multi-index  $i_m^k$  is used to denote the index of the  $\alpha$  ( $\beta$ ) spin orbital that is in position  $m$  ( $n_\alpha + m$ ) in the  $k$ th Slater determinant  $\Theta_k$ .

The overlap between two states  $\psi_I$  and  $\psi'_J$  is then given by

$$\langle\psi_I|\psi'_J\rangle = \sum_{k=1}^{N_I} \sum_{l=1}^{N'_J} C_{kI} C'_{lJ} \langle\Theta_k|\Theta'_l\rangle. \quad (19)$$

The bottleneck in the evaluation of Equation 19 is the calculation of the overlaps between the Slater determinants in the sets  $\{\Theta_k\}$  and  $\{\Theta'_k\}$ , which are given by the determinant of the matrix of overlaps between the spin orbitals occupied in the two Slater determinants:

many orders of magnitude can be attained. Our approach is based on the algorithm reported in Reference 31, but with two key modifications.

Firstly, we note that common  $\alpha$  and  $\beta$  spin orbital occupations occur not just between pairs of wavefunctions  $\psi_I$  and  $\psi'_J$ , but between sets of wavefunctions  $\{\psi_I\}$  and  $\{\psi'_I\}$ . Thus, we identify, precompute and store all unique factors  $\det(\mathbf{s}_{kl})$  and  $\det(\bar{\mathbf{s}}_{kl})$  based on the common  $\alpha$  and  $\beta$  spin orbital occupations across all states in the sets  $\{\psi_I\}$  and  $\{\psi'_I\}$ . In the P-BDD procedure,  $n_{state}^2$  wavefunction overlaps have to be computed, where  $n_{state}$  is the number of electronic states being considered. For even moderate numbers of states, precomputing the unique factors across all pairs of states, instead of on a pair-by-pair basis, can result in significant computational savings.

Secondly, we recognise that many of the unique factors

$\det(\mathbf{s}_{kl})$  and  $\det(\bar{\mathbf{s}}_{kl})$  will be very small in magnitude and can, in fact, be neglected without detriment. We thus introduce a screening step in the generation of the unique factors  $\det(\mathbf{s}_{kl})$  and  $\det(\bar{\mathbf{s}}_{kl})$ . This requires a fast, robust estimate of the magnitude of a determinant. For this we make use of Hadamard's inequality, which, for a matrix  $\mathbf{X} \in \mathbb{R}^{m \times m}$ , reads

$$|\det(\mathbf{X})|^2 \leq \prod_{i=1}^m \|\mathbf{x}_i\|^2, \quad (21)$$

where  $\mathbf{x}_i$  are the columns of  $\mathbf{X}$ . The calculation of the bound Equation 21 scales as  $\mathcal{O}(m^2)$ , whereas the calculation of the determinant scales as  $\mathcal{O}(m^3)$ . For the factors  $\det(\mathbf{s}_{kl})$  and  $\det(\bar{\mathbf{s}}_{kl})$ , the matrix dimension,  $m$ , is  $n_\alpha$  and  $n_\beta$ , respectively. Thus, if many of the factors are small enough to be neglected, then screening these using Hadamard's inequality will lead to a considerable speedup. We refer to this screening step as Hadamard screening.

Lastly, we also consider the use of truncation as a way to speed up the computation of the wavefunction overlaps. In particular, a norm-based truncation is used in which the replacement

$$\psi_I = \sum_{k=1}^{N_I} C_{kI} \Theta_k \rightarrow \tilde{\psi}_I = \sum_{k \in \mathcal{S}_I} \tilde{C}_{kI} \Theta_k, \quad (22)$$

$$\tilde{C}_{kI} = \sqrt{\sum_{k \in \mathcal{S}_I} C_{kI}^2}, \quad (23)$$

is made. Here,  $\mathcal{S}_I$  is the smallest subset of Slater determinant indices that yields a truncated wavefunction with a norm above a given threshold  $\delta_t$  for the  $I$ th state.

### III. METHODOLOGY

#### A. Calculation of the vibronic absorption spectrum of pyrazine

As part of our analysis of the quality of the diabatic potentials yielded by the DFT/MRCI P-BDD method, we explored the construction of model potentials for use in the simulation of vibronic spectra. The test case chosen was the absorption spectrum of pyrazine. This is an often-used benchmark system for the study of vibronic coupling effects in absorption spectra, with a proper description of the strong coupling between its first two excited states being necessary for the correct reproduction of the absorption spectrum.

Let  $\sigma_I(E)$  denote the absorption spectrum corresponding to vertical excitation from the ground state to the excited diabatic electronic state  $\phi_I(\mathbf{r}; \mathbf{R})$ .  $\sigma_I(E)$  may be calculated within a time-dependent framework from the

Fourier transform of the autocorrelation function  $a_I(t)$  corresponding to an initial wavepacket  $|\Psi(t)\rangle$  prepared by vertical excitation to  $\phi_I(\mathbf{r}; \mathbf{R})$ :

$$\sigma_I(E) \propto E \int_{-\infty}^{\infty} a_I(t) \exp(iEt) dt, \quad (24)$$

with

$$a_I(t) = \langle \Psi(0) | \Psi(t) \rangle, \quad (25)$$

$$|\Psi(0)\rangle = \{|\phi_I\rangle \langle \phi_1| + h.c.\} |\Psi_{GS}\rangle. \quad (26)$$

Here,  $|\Psi_{GS}\rangle$  denotes the ground vibronic state, which was obtained *via* wavepacket relaxation[32].

All wavepacket propagations were performed using the multiconfigurational time-dependent Hartree (MCTDH) approach[33–35], as implemented in the Quantics quantum dynamics package[36]. The multi-set formalism was used, in which the wavefunction *ansatz* reads

$$|\Psi(\mathbf{q}, t)\rangle = \sum_{I=1} |\Psi^{(I)}(\mathbf{q}, t)\rangle |\phi_I\rangle. \quad (27)$$

Here,  $|\Psi^{(I)}(\mathbf{q}, t)\rangle$  is the nuclear wavefunction for the  $I$ th electronic state, which is expanded in a direct product basis formed from time-dependent functions  $\varphi_{j_k}^{(\kappa, I)}$ , termed single-particle functions (SPFs):

$$|\Psi^{(I)}(\mathbf{q}, t)\rangle = \sum_{j_1^I=1}^{n_1^I} \cdots \sum_{j_p^I=p}^{n_p^I} A_{j_1^I, \dots, j_p^I}^{(I)}(t) \prod_{\kappa=1}^p \varphi_{j_k^I}^{(\kappa, I)}(q_\kappa, t). \quad (28)$$

The SPFs are functions of generally multi-dimensional logical coordinates  $q_\kappa$ , each corresponding to a composite of  $d_\kappa$  physical nuclear coordinates  $R_\nu^{(\kappa)}$ :

$$q_\kappa = \left( R_1^{(\kappa)}, \dots, R_{d_\kappa}^{(\kappa)} \right). \quad (29)$$

The time-dependent SPFs are further expanded in terms of a time-independent discrete variable representation (DVR)[34, 37]. Equations of motion for both the expansion coefficients  $A_{j_1^I, \dots, j_p^I}^{(I)}$  and the SPFs are derived variationally, yielding an optimal description of the evolving wavepacket[34].

In order to perform the MCTDH wavepacket propagations, the molecular Hamiltonian is represented in terms of the quasi-diabatic states  $\{\phi_I(\mathbf{r}; \mathbf{R})\}$  furnished by the DFT/MRCI P-BDD calculations:

$$\begin{aligned}
\hat{H} &= \sum_{IJ} |\phi_I(\mathbf{r}; \mathbf{R})\rangle \langle \phi_I(\mathbf{r}; \mathbf{R})| \hat{H} |\phi_J(\mathbf{r}; \mathbf{R})\rangle \langle \phi_J(\mathbf{r}; \mathbf{R})| \\
&= \sum_I |\phi_I(\mathbf{r}; \mathbf{R})\rangle \hat{T}_n(\mathbf{R}) \langle \phi_I(\mathbf{r}; \mathbf{R})| \\
&+ \sum_{IJ} |\phi_I(\mathbf{r}; \mathbf{R})\rangle W_{IJ}(\mathbf{R}) \langle \phi_J(\mathbf{r}; \mathbf{R})|.
\end{aligned} \tag{30}$$

where the  $W_{IJ}(\mathbf{R}) = \langle \phi_I | \hat{H}_{el} | \phi_J \rangle$  are the elements of the quasi-diabatic potential matrix  $\mathbf{W}(\mathbf{R})$ . To proceed,  $\mathbf{W}(\mathbf{R})$  must be re-cast in a form that is compatible with MCTDH. Specifically, as a sum of products of monomodal operators[34]. This is achieved by approximating  $\mathbf{W}(\mathbf{R})$  using the vibronic coupling Hamiltonian model of Köppel *et al.*[38, 39]. Briefly,  $\mathbf{W}(\mathbf{R})$  is represented by a Taylor expansion in terms of mass- and frequency-scaled normal modes,  $Q_\alpha$ , about the ground state minimum  $\mathbf{Q}_0$ . Our model potential is complete up to fourth-order in the one-mode terms and contains only bi-linear two-mode terms:

$$\begin{aligned}
W_{IJ}(\mathbf{R}) &\approx W_{IJ}^{mod}(\mathbf{Q}) \\
&= \tau_0^{(I,J)} + \sum_{p=1}^4 \frac{1}{p!} \sum_{\alpha} \tau_{p\alpha}^{(I,J)} Q_\alpha^p + \frac{1}{2} \sum_{\alpha\beta} \eta_{\alpha\beta}^{(I,J)} Q_\alpha Q_\beta.
\end{aligned} \tag{31}$$

The coupling coefficients  $\tau_p^{(I,J)}$  and  $\eta^{(I,J)}$  were calculated using a normal equations approach, as detailed in Appendix A.

We note that, although only approximations to the functions of interest, if the model potentials used yield accurate absorption spectra, then it can be concluded that the DFT/MRCI P-BDD potentials to which they are fitted are of good quality, which is what we aim to establish.

## B. Quantum Chemistry Calculations

In all DFT/MRCI calculations, the R2016 Hamiltonian was used[2]. The parameterisation of this Hamiltonian was performed using the BH-LYP functional, and, accordingly, this was used in all calculations. The KS orbitals used were computed using the Turbomole set of programs[40].

For the pyrazine calculations, the TZVP basis was used in all DFT/MRCI calculations. In the construction of the vibronic coupling Hamiltonian, normal modes and frequencies were calculated at the MP2/TZVP level of theory. Both the geometry optimisation and frequency calculations were performed using the Turbomole set of programs[40].

In the LiH calculations, the QZVPP basis set was used. In addition to the DFT/MRCI calculations, canonical MRCI calculations were also performed to provide benchmark derivative coupling values. In these calculations, a

(2,5) active space comprised of the  $1s_H$ ,  $2s_{Li}$ , and the full set of  $2p_{Li}$  orbitals was used. These calculations were performed using the Columbus set of programs[41].

## IV. RESULTS

We here present the results of P-BDD calculations performed using DFT/MRCI wavefunctions.

In Section IV A, we discuss the diabatic potentials calculated for the two lowest-lying  $1\Sigma^+$  states of LiH using the combination of the DFT/MRCI and P-BDD methodologies. In Section IV B, we consider the results of spectral simulations performed for pyrazine using a model potential derived from DFT/MRCI P-BDD calculations. We also present an analysis of the sensitivity of the wavepacket propagation to the errors introduced into the P-BDD diabatic potentials through the use of different levels of approximation. Namely, Hadamard screening and wavefunction truncation.

### A. LiH

The  $1^1\Sigma^+$  and  $2^1\Sigma^+$  adiabatic states of LiH display an ionic-covalent avoided crossing as the Li-H bond is stretched. At the equilibrium bond length, the  $1^1\Sigma^+$  state has an ionic  $(1s_{Li})^2(1s_H)^2$  character, while the  $2^1\Sigma^+$  state has  $(1s_{Li})^2(1s_H)(2s_{Li})$  character. The two states, however, are strongly coupled by the Li-H stretching coordinate, resulting in a pronounced avoided crossing and the mixing of the state characters as the bond is elongated.

For clarity, the following state labeling convention shall be used. The adiabatic states of interest will be labeled by the term symbols  $1^1\Sigma^+$  and  $2^1\Sigma^+$ . The diabatic states derived from these shall be labeled by  $\tilde{X}$  and  $\tilde{A}$ .

#### 1. Adiabatic and Diabatic Potentials

Using the P-BDD diabatisation procedure, the  $1^1\Sigma^+$  and  $2^1\Sigma^+$  states were rotated to a diabatic representation. In the P-BDD calculations, the adiabatic and diabatic representations were taken to be equal at the  $1^1\Sigma^+$  minimum energy bond length, denoted by  $r_0$ . Owing to the small size of the problem, no approximations (wavefunction truncation and Hadamard screening) were used in the P-BDD calculations.

The calculated adiabatic and diabatic potentials are shown in Figure 1. Also shown in Figure 1 is the diabatic coupling,  $W_{12}$ , between the  $\tilde{X}$  and  $\tilde{A}$  states as a function of bond length. The DFT/MRCI P-BDD diabatic potential is found to capture the strong non-adiabatic coupling between the  $1^1\Sigma^+$  and  $2^1\Sigma^+$  states, with the avoided crossing being correctly removed in the diabatic representation.

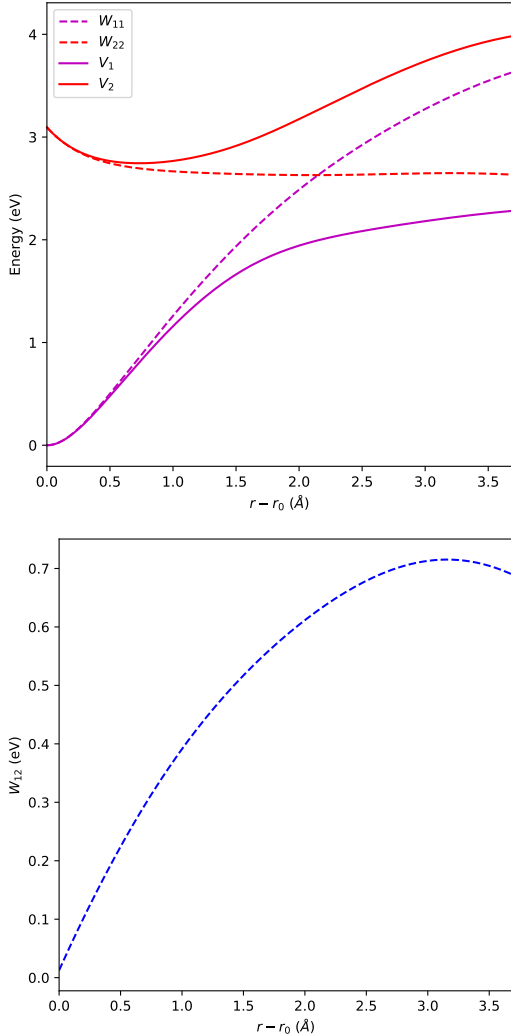


FIG. 1: Top: Adiabatic and diabatic potential energy surfaces for the first two  $1^1\Sigma^+$  states of LiH calculated at the DFT/MRCI/QZVPP level of theory. Bottom: diabatic coupling between the  $\tilde{X}$  and  $\tilde{A}$  states, also calculated at the DFT/MRCI/QZVPP level of theory. All diabatic quantities were calculated using the P-BDD method.

## 2. Derivative Couplings

Further, more conclusive evidence that the DFT/MRCI P-BDD diabatic potentials correctly account for the non-adiabatic coupling of the  $1^1\Sigma^+$  and  $2^1\Sigma^+$  states comes from a consideration of the derivative coupling,  $F_{12}(r)$ , between the two states as derived from the DFT/MRCI P-BDD diabatic potential  $\mathbf{W}(r)$ ,

$$F_{12}(r) = \left\langle \psi_1(r) \left| \frac{\partial}{\partial r} \right| \psi_2(r) \right\rangle = \frac{\left[ \mathbf{U}(r) \frac{\partial \mathbf{W}(r)}{\partial r} \mathbf{U}^\dagger(r) \right]_{12}}{V_2(r) - V_1(r)}, \quad (32)$$

where  $\mathbf{U}$  denotes the P-BDD ADT matrix and  $V_I$  its eigenvalues. To determine the derivatives of the diabatic potential matrix elements  $W_{IJ}$ , the calculated values were first fitted to a tenth-order Chebyshev expansion that was then analytically differentiated. To provide a benchmark to compare to, derivative couplings were also calculated analytically at the canonical MRCI level of theory.

The DFT/MRCI P-BDD and canonical MRCI derivative couplings are shown alongside each other in Figure 2. Importantly, it is found that the DFT/MRCI P-BDD derivative couplings behave similarly to the canonical MRCI values as a function of Li-H bond length. In particular, the maximum value reached ( $0.51 E_h \text{Å}^{-1}$ ) compares very agreeably with the maximum value of the canonical MRCI derivative couplings ( $0.49 E_h \text{Å}^{-1}$ ). The one slight discrepancy between the two results is that the DFT/MRCI P-BDD values peak around  $0.5 \text{Å}$  before the MRCI values, a result of the DFT/MRCI method yielding an avoided crossing between the  $1^1\Sigma^+$  and  $2^1\Sigma^+$  states that is slightly too early compared to the MRCI result. If, however, the DFT/MRCI P-BDD and canonical MRCI derivative couplings are plotted as a function of displacement from the centre of the avoided crossing,  $r_c$ , then almost quantitative agreement is found, as shown in Figure 2.

## 3. Natural Orbital Analysis of Ionic and Covalent State Characters

Finally, we consider the characters of the DFT/MRCI P-BDD diabatic states as a function of the Li-H bond length. Unlike in the adiabatic representation, the  $\tilde{X}$  and  $\tilde{A}$  states should maintain ionic and covalent characters, respectively, as the Li-H bond is stretched (so long as the bond length  $r$  is within the non-asymptotic region of the potential). To analyse the electronic characters of the diabatic states at a given bond length, we consider the dominant natural orbitals (NOs) derived from the density matrices constructed using the DFT/MRCI P-BDD diabatic wavefunctions. Remembering that the electronic density  $\rho(\mathbf{r})$  for a given state can be expressed in terms of NOs  $\varphi_p$  and natural occupations  $\lambda_p$  as

$$\rho(\mathbf{r}) = \sum_p \lambda_p |\varphi_p|^2, \quad (33)$$

the spatial (de)localisation of the dominant NOs can be used to assess the degree of ionic versus covalent character of a given electronic state.

We first consider the  $1^1\Sigma^+$  and  $2^1\Sigma^+$  state NOs at the equilibrium bond length,  $r_0$ , where these states have,

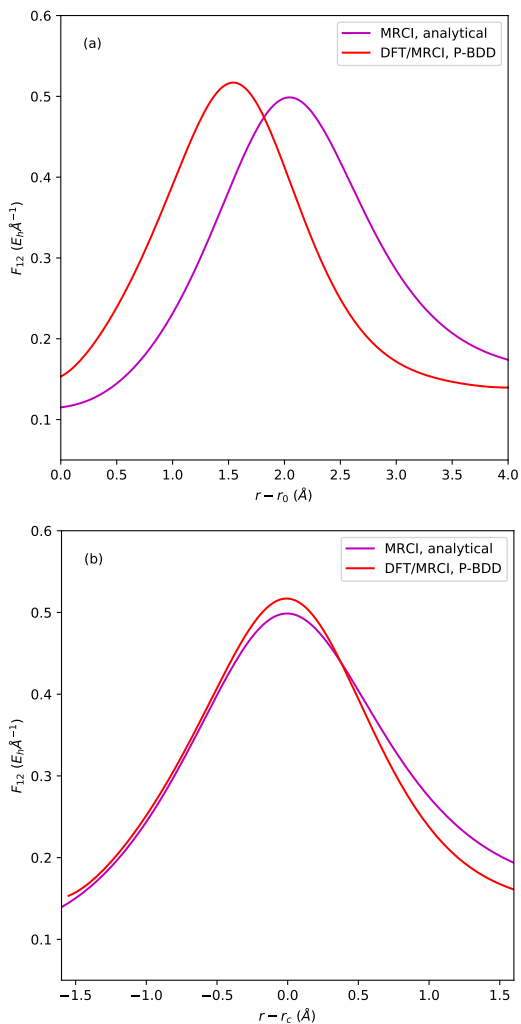


FIG. 2: Comparison of derivative coupling terms  $F_{12}(r)$  between the first two  $1^1\Sigma^+$  states of LiH calculated from the DFT/MRCI P-BDD diabatic potential matrix and analytically at the MRCI(2,6) level of theory. (a) Comparison of  $F_{12}$  values as a function of Li-H bond length. (b) Comparison of  $F_{12}$  values as a function of the displacement from the centre of the avoided crossing between the  $1^1\Sigma^+$  and  $2^1\Sigma^+$  states,  $r_c$ . The QZVPP basis was used in all calculations.

respectively, ionic and covalent characters. These are shown in Figure 3. The ionic character of the  $1^1\Sigma^+$  state at  $r_0$  is clearly reflected in the NOs: only two NOs exist with non-zero natural occupations, corresponding each to a  $1s_{Li}$  and  $1s_H$  type orbital. Both have natural occupations of 2.0. This corresponds, loosely speaking, to a net partial positive charge associated with the Li-atom and a net partial negative charge associated with the H-atom (owing to their different nuclear charges). On the other hand, the NOs for the  $2^1\Sigma^+$  state show an increase in the localisation of the electron density over the Li-atom, with the doubly-occupied  $1s_H$  NO being replaced

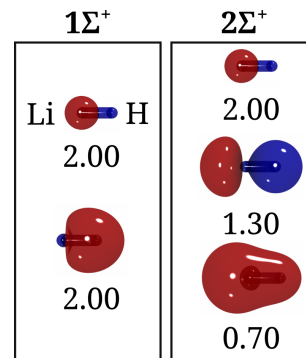


FIG. 3: Natural orbitals for  $1^1\Sigma^+$  and  $2^1\Sigma^+$  states at the equilibrium bond length,  $r_0$ , calculated at the DFT/MRCI/QZVPP level of theory. The numbers below each natural orbital is the corresponding natural occupation. For the first NO for the  $1^1\Sigma^+$  state, the Li and H atom labels are also given.

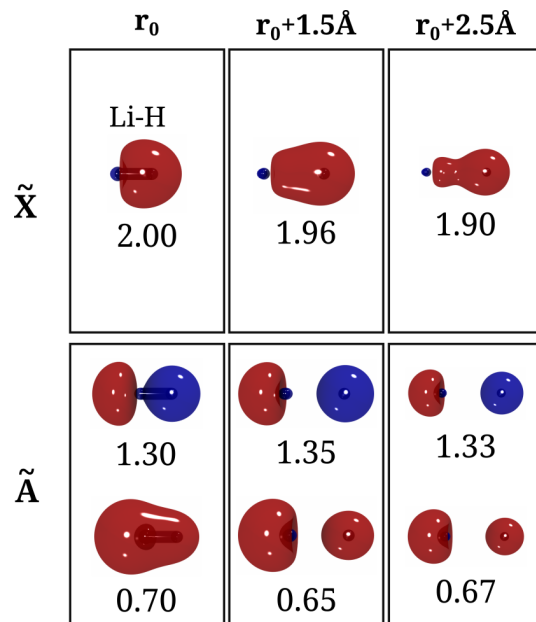


FIG. 4: Diabatic natural orbitals for  $\tilde{X}$  and  $\tilde{A}$  states of LiH as a function of bond length calculated at the DFT/MRCI/QZVPP P-BDD level of theory. Here,  $r_0$  denotes the equilibrium bond length. The numbers below each natural orbital is the corresponding natural occupation. Excluded are the NOs corresponding to the  $1s_{Li}$  orbital.

with two fractionally-occupied NOs corresponding to linear combinations of the  $2s_{Li}$  and  $1s_H$  orbitals. This can be clearly be seen to correspond to a more valence-type electronic character.

Next, we consider the NOs for the  $\tilde{X}$  and  $\tilde{A}$  states as a function of the Li-H bond length. The dominant NOs at different L-H bond lengths are shown in Figure



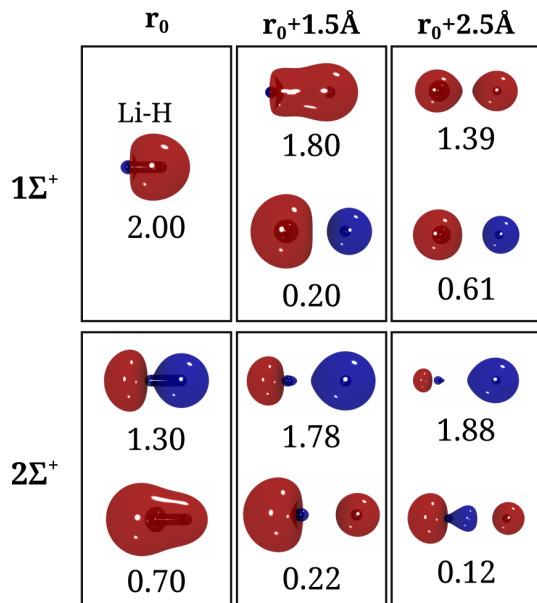


FIG. 5: Adiabatic natural orbitals for  $1^1\Sigma^+$  and  $2^1\Sigma^+$  states of LiH as a function of bond length calculated at the DFT/MRCI/QZVPP level of theory. Here,  $r_0$  denotes the equilibrium bond length. The numbers below each natural orbital is the corresponding natural occupation. Excluded are the NOs corresponding to the  $1s_{Li}$  orbital.

4 along with the corresponding natural occupations. As the occupied NO corresponding to the  $1s_{Li}$  orbital remains virtually unchanged in character and occupation, it is omitted. At the equilibrium bond length,  $r_0$ , the adiabatic and diabatic representations are equal, yielding  $\tilde{X}$  and  $\tilde{A}$  states with ionic and covalent character, respectively. From the NOs at elongated Li-H bond lengths of  $r_0+1.5 \text{ \AA}$  and  $r_0+2.5 \text{ \AA}$ , it can clearly be seen that the  $r_0$  ionic and covalent characters of the  $\tilde{X}$  and  $\tilde{A}$  states are preserved, as they should be for good diabatic states. In contrast the NOs for the  $1^1\Sigma^+$  and  $2^1\Sigma^+$  states (shown in Figure 5) show that the pure ionic and covalent characters of the adiabatic states is lost, as a result of their non-adiabatic coupling, as the Li-H bond is elongated. Particularly striking is loss of ionic character of the  $1^1\Sigma^+$  adiabatic state: at  $r_0+1.5 \text{ \AA}$ , the dominant (non- $1s_{Li}$ ) NOs clearly have non-zero values around the Li atom, and at  $r_0+2.5 \text{ \AA}$  the  $2^1\Sigma^+$  has developed essentially pure covalent character.

## B. Pyrazine Absorption Spectrum Simulation

A total of three electronic states were included in the P-BDD calculations: the  $1B_{3u}(n\pi^*)$ ,  $1B_{2u}(\pi\pi^*)$  and  $1A_u(n\pi^*)$  states. The Franck-Condon point vertical excitation energies and oscillator strengths of these states at the DFT/MRCI/TZVP level of theory are given in Table

TABLE I: Franck-Condon point vertical excitation energies,  $\Delta E$ , and oscillator strengths,  $f$ , for the first three excited states of pyrazine calculated at the DFT/MRCI level of theory using the TZVP basis. All energies are given in units of eV.

State	$\Delta E$	$f$
$1B_{3u}(n\pi^*)$	4.09	0.012
$1B_{2u}(\pi\pi^*)$	4.87	0.116
$1A_u(n\pi^*)$	5.05	0.000

TABLE II: Combined modes, and primitive and SPF basis dimensions used in the MCTDH simulations of the pyrazine  $1B_{2u}(\pi\pi^*)$  state absorption spectrum. For all modes, a harmonic oscillator DVR was used as the primitive basis. The numbers  $N_i$  are primitive basis sizes for each physical coordinate. The numbers  $n_1, n_2, n_3$  are the SPF basis sizes for each combined mode in the  $1B_{3u}(n\pi^*)$ ,  $1B_{2u}(\pi\pi^*)$  and  $1A_u(n\pi^*)$  states, respectively.

Mode	$N_i, N_j$	$n_1, n_2, n_3$
$Q_2, Q_{6a}$	10,48	15,12,12
$Q_1$	32	12,12,12
$Q_{8a}, Q_{9a}$	36,22	14,12,12
$Q_{8b}, Q_{10a}$	22,22	12,12,12

I. To provide direct comparison with previous studies of pyrazine's absorption spectrum, we adopt the commonly used normal mode nomenclature of Innes *et al.*[42].

In the MCTDH calculations, a propagation time of 120 fs was used, yielding the wavepacket autocorrelation function for 240 fs[43]. The primitive and SPF basis information is given in Table II. Seven modes were included. These are the five totally symmetric ( $a_g$ ) modes  $Q_1, Q_2, Q_{6a}, Q_{8a}$ , and  $Q_{9a}$ . Additionally, the coupling modes  $Q_{8b}$  and  $Q_{10a}$  were also included. The mode  $Q_{10a}$  strongly couples the  $1B_{3u}(n\pi^*)$  and  $1B_{2u}(\pi\pi^*)$  states, whilst the  $Q_{8b}$  mode is responsible for significant coupling of the  $1B_{3u}(n\pi^*)$  and  $1A_u(n\pi^*)$  states. For reference, we show the calculated DFT/MRCI P-BDD diabatic potentials along these modes in Figure 6. Also shown in here are the model potentials fitted to the DFT/MRCI P-BDD diabatic potentials. Excellent agreement between the calculated and model potential values is found along these cuts. We can thus state with confidence that the accuracy of the absorption spectrum calculated using the model diabatic potential  $\mathbf{W}^{mod}(\mathbf{Q})$  can be used to assess the quality of the DFT/MRCI P-BDD diabatic potentials to which it is fitted.

Shown in Figure 7 is the absorption spectrum calculated following vertical excitation to the bright  $1B_{2u}(\pi\pi^*)$  state. For comparison, we also show the experimental spectrum of Reference 44, taken from the Mainz spectral database[45]. To account for homo-

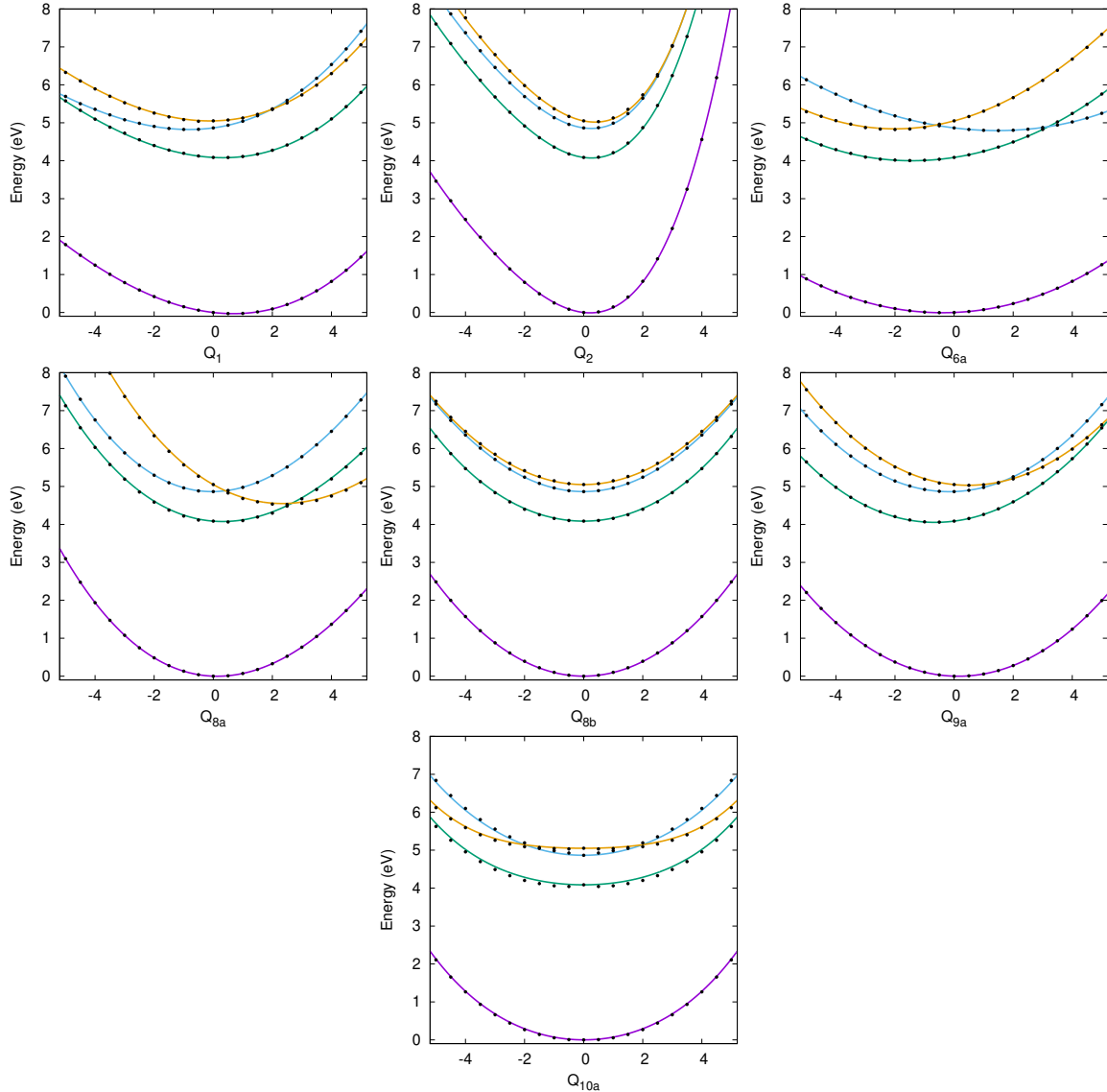


FIG. 6: P-BDD diabatic potentials calculated at the DFT/MRCI/TZVP level of theory for the first four electronic states in pyrazine. The calculated potential values are given by the black dots, whilst the solid lines give the model potential values.

geneous broadening present in the experimental spectrum, the calculated spectrum was convoluted with a Lorentzian lineshape with a full width at half maximum (FWHM) of 40 meV. Overall, excellent agreement between the calculated and experimental spectra is found. This both validates the model diabatic potential used in its simulation, as well as the underlying DFT/MRCI P-BDD calculations. This is an important result, as in order to reproduce the experimental spectrum, the non-adiabatic coupling between the  $1B_{3u}(n\pi^*)$  and  $1B_{2u}(\pi\pi^*)$  states must be correctly described[46–49].

### C. Approximations in the P-BDD calculations

Having established that the combination of DFT/MRCI and P-BDD is capable of yielding accurate diabatic potentials, we now consider the effects of various levels of approximation that may be made in the P-BDD procedure in order to decrease computational costs. Given two sets of neighboring adiabatic wavefunctions  $\{\psi_I(\mathbf{r}; \mathbf{R}_n)\}$  and  $\{\psi_I(\mathbf{r}; \mathbf{R}_{n+1})\}$ , the bottleneck in a P-BDD calculation is in the computation of all overlaps between the members of the two sets. Here, two approximations may be made: (i) Hadamard screening of the unique factors  $\det(\mathbf{s}_{kl})$  and  $\det(\bar{\mathbf{s}}_{kl})$ , and; (ii) the truncation of the Slater determinant expansions of the

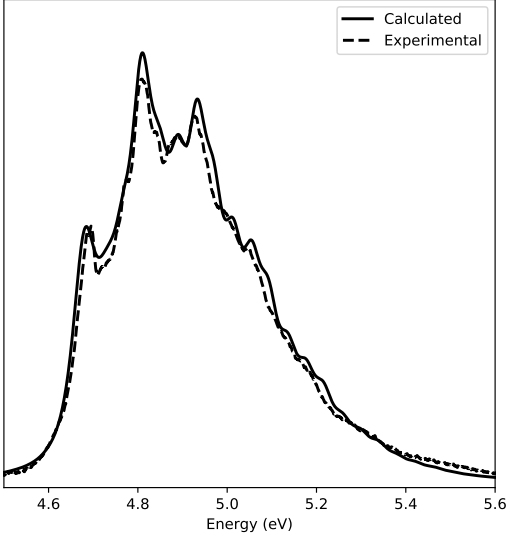


FIG. 7: Absorption spectrum corresponding to vertical excitation to the  $1B_{2u}(\pi\pi^*)$  state of pyrazine calculated using the four-state, seven-mode model potential fitted to diabatic potentials calculated using DFT/MRCI and P-BDD with the TZVP basis. Shown alongside for comparison is the experimental spectrum[44].

wavefunctions  $\psi_I(\mathbf{r}; \mathbf{R})$ . We are ultimately interested in the use of DFT/MRCI P-BDD diabatic potentials in quantum dynamics simulations. Therefore, we consider the changes in the wavepacket autocorrelation function  $a(t)$  in the pyrazine MCTDH calculation performed using model potentials derived from DFT/MRCI P-BDD calculations using different Hadamard screening thresholds and wavefunction truncations. For reference, we show in Figure 8 (a) the absolute value  $|a(t)|$  of the wavepacket autocorrelation function calculated following vertical excitation to the  $1B_{2u}(\pi\pi^*)$  state of pyrazine with the same four-state, seven-mode model used in the spectrum simulations. Shown in Figure 8 (b) are the differences in  $|a(t)|$ , relative to the exact overlap results, calculated using various levels of approximation.

We first consider the effects of Hadamard screening in the calculation of wavefunction overlaps in the P-BDD calculations. Two levels of approximations were used, corresponding to Hadamard screening thresholds  $\delta_H$  of  $10^{-6}$  and  $10^{-4}$ . As can be seen in Figure 8 (b), the effect of using a Hadamard screening threshold  $\delta_H = 10^{-6}$  has an effect on the autocorrelation function that is of the order of machine precision. Increasing  $\delta_H$  to  $10^{-4}$  increases the error in the autocorrelation function, but the maximum error for times up to 240 fs is only  $\mathcal{O}(10^{-6})$ , which is still negligible. The Hadamard screening of unique factors in the P-BDD calculations does, however, result in savings in computational costs, as shown in Figure 9 (a). Here, the timings for the P-BDD calculations are shown for the exact calculations (no screening), and Hadamard

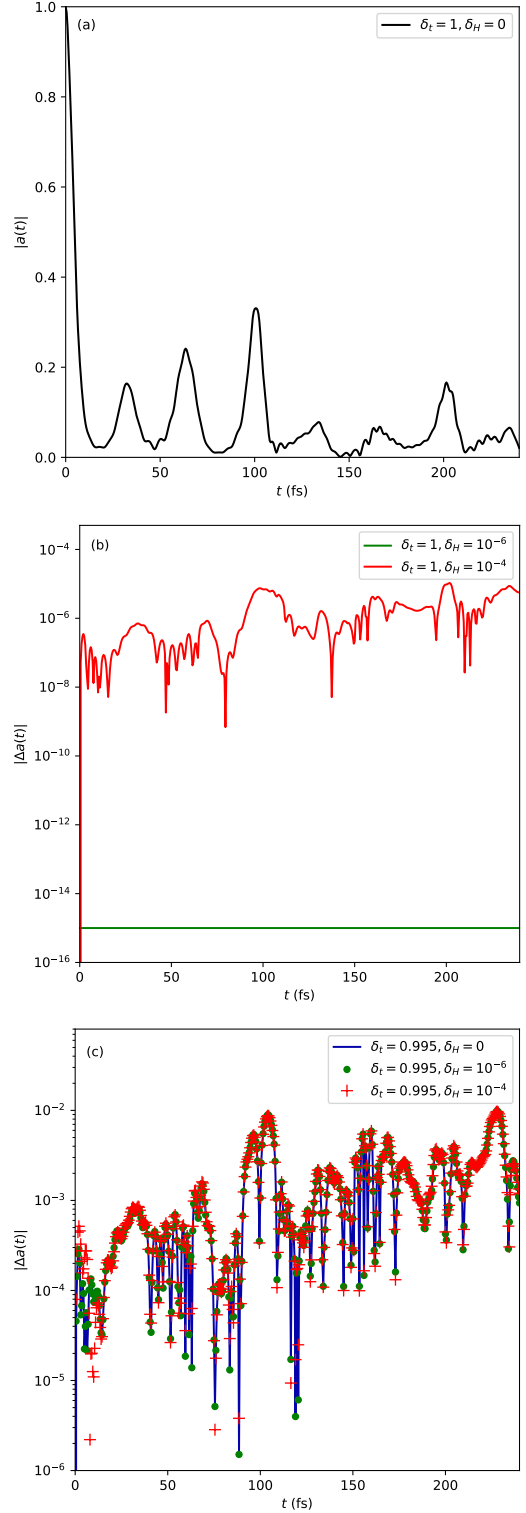


FIG. 8: Autocorrelation functions calculated following vertical excitation to the  $1B_{2u}(\pi\pi^*)$  state of pyrazine using the four-state, seven-mode model potential fitted to diabatic potentials calculated using DFT/MRCI and P-BDD. (a) Autocorrelation function obtained from potentials calculated using P-BDD with exact wavefunction overlaps. (b) Differences in the autocorrelation functions calculated using P-BDD with different Hadamard screening thresholds,  $\delta_H$ , and untruncated wavefunctions. (c) Differences in the autocorrelation functions calculated using P-BDD with different Hadamard screening thresholds,  $\delta_H$ , and a norm truncation threshold  $\delta_t = 0.995$ .

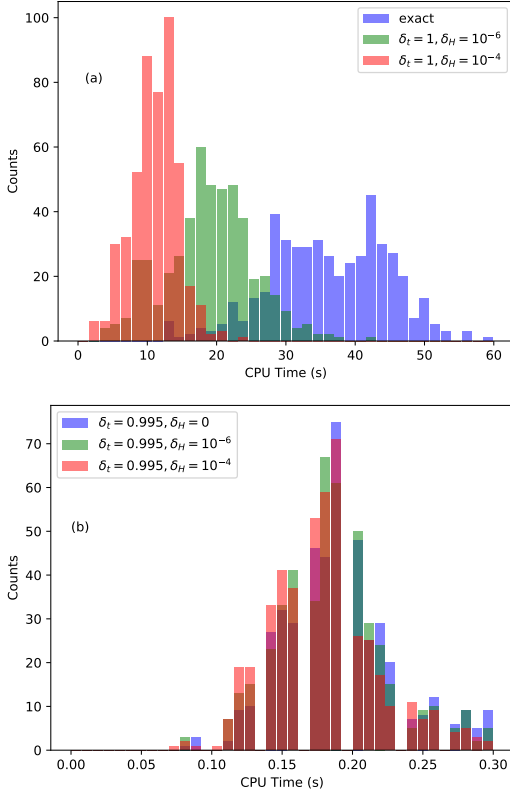


FIG. 9: Timings for the P-BDD calculations for pyrazine using four electronic states calculated at the DFT/MRCI level of theory using the TZVP basis. (a) Timings for different screening thresholds  $\delta_H$  and untruncated wavefunctions. (b) Timings for wavefunctions truncated using a norm truncation threshold  $\delta_t = 0.995$  and different screening thresholds  $\delta_H$ . All timings correspond to the use a single Intel i7-6700K CPU core.

screening thresholds of  $\delta_H = 10^{-6}$  and  $\delta_H = 10^{-4}$ . Note that because the DFT/MRCI method employs an adaptive configuration selection algorithm[1], the numbers of Slater determinants, and hence the computational cost of each P-BDD calculation, varies from geometry to geometry. It can clearly be seen that the use of Hadamard screening leads to significant savings in computational costs: the average timing for the P-BDD calculations performed with no screening,  $\delta_H = 10^{-6}$  and  $\delta_H = 10^{-4}$  are 39, 19 and 11 seconds, respectively. Considering the negligible loss in accuracy resulting from the Hadamard screening procedure, these can be deemed to be worthwhile savings.

Secondly, we examine the effects of wavefunction truncation in the P-BDD calculations on the wavepacket autocorrelation function. To do so, the P-BDD calculations were performed using wavefunction expansions truncated to give wavefunction norms  $||\psi_I||$  of 0.995. The effect of wavefunction truncation on the error in the autocorrela-

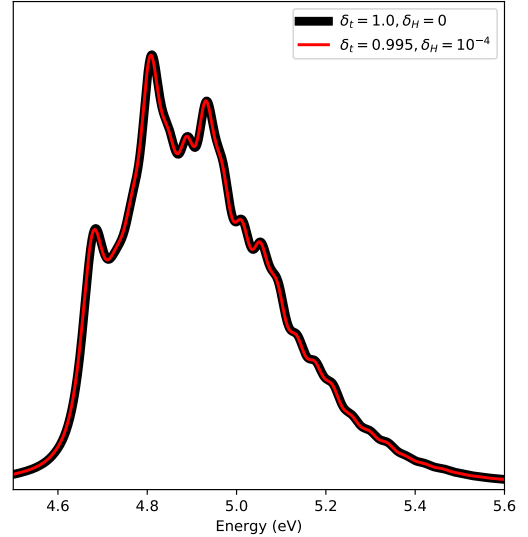


FIG. 10: Absorption spectrum corresponding to vertical excitation to the  $1B_{2u}(\pi\pi^*)$  state of pyrazine calculated using the four-state, seven-mode model and different levels of approximation in the P-BDD diabatization calculations. Thick black line: exact P-BDD calculations. Thin red line: norm truncation threshold  $\delta_t = 0.995$  and Hadamard screening threshold  $\delta_H = 10^{-4}$ .

tion function is more pronounced than for the introduction of Hadamard screening, as can be seen in Figure 8 (b). However, even up to 240 fs, the errors in the autocorrelation function are still relatively small. Also shown here are the errors in the autocorrelation function obtained when using a combination of wavefunction truncation and Hadamard screening. As may be expected, the errors resulting from the combination of wavefunction truncation and Hadamard screening are of the same order of magnitude as for wavefunction truncation alone. Finally, we show in Figure 9 (b) the timings for the P-BDD calculations performed using truncated wavefunction expansions. Relative to the untruncated results (shown in Figure 9 (a)), the results are striking, with a speed up by two orders of magnitude being attained, and all calculations now taking less than 0.3 seconds. In fact, with a norm threshold of 0.995, the calculation of the wavefunction overlaps no longer dominates the total P-BDD calculation, as can be seen by the very similar timings for the  $\delta_H = 0$ ,  $\delta_H = 10^{-6}$ , and  $\delta_H = 10^{-4}$  calculations.

Clearly, the use of Hadamard screening and wavefunction truncation both lead to considerable speedups in a P-BDD calculation. In the case of Hadamard screening, we observe that even a relatively loose screening threshold ( $\delta_H = 10^{-4}$ ) leads to decreases in computation cost of around 70% with negligible effects on the accuracy of the diabatic potentials. Wavefunction truncation leads to even greater computational savings, by orders of mag-

nitude. Here, the degradation of the accuracy of the P-BDD diabatic potentials is found to be greater, but is found to still be small enough to justify the use of this approximation. To demonstrate this, we show in Figure 10 the absorption spectrum calculated using model potentials derived from P-BDD calculations employing no approximations ( $\delta_t = 1.0$ ,  $\delta_H = 0$ ) and with both norm truncation and a loose Hadamard screening threshold ( $\delta_t = 0.995$ ,  $\delta_H = 10^{-4}$ ). The two spectra are found to be barely distinguishable from each other, lending justification to this level of approximation.

## V. CONCLUSIONS

The DFT/MRCI method is a well established tool for the calculation of the excited states of large molecular systems. The excellent cost-to-accuracy ratio of DFT/MRCI makes it an appealing choice for the construction of excited state potentials and non-adiabatic couplings for use in quantum dynamics simulations. The lack of analytical derivative couplings within DFT/MRCI means that one must adopt a diabatic representation in order to achieve this. The challenge, then, is to determine a diabatisation procedure that is compatible with DFT/MRCI. Due to the lack of analytical derivative couplings and the constraint of having to use canonical KS MOs as the single-particle basis, this a non-trivial task.

Our solution to this problem is to use a propagative variant of the BDD method of Pacher, Cederbaum and Köppel[17, 18, 24], termed P-BDD. The P-BDD method is both formally rigorous and requires as input only the overlaps of sets of electronic wavefunctions at neighboring nuclear geometries, which are amenable to computation at the DFT/MRCI level of theory.

The bottleneck in a P-BDD calculation is the determination of large numbers of wavefunction overlaps in terms of non-orthogonal sets of MOs. To render this computationally tractable, we implemented the recently reported algorithm of Plasser *et al.*[31] with two key modifications. Firstly, common factors (unique determinants of spin orbital overlaps) were determined and stored not just on a wavefunction-pair basis, but for all wavefunction pairs simultaneously. Secondly, the use of Hadamard screening of the unique factors was introduced. Using these modifications, large numbers of wavefunction overlaps can be computed efficiently, making the P-BDD procedure tractable even for large molecules and many electronic states.

As an initial application of the DFT/MRCI P-BDD method, diabatic potentials were calculated for LiH and pyrazine. For LiH, the DFT/MRCI P-BDD diabatic potentials were found to correctly capture the strong non-adiabatic coupling between the  $1^1\Sigma^+$  and  $2^1\Sigma^+$  states. In particular, the derivative couplings derived from the DFT/MRCI P-BDD diabatic potential matrix were found to compare well to those calculated analytically using canonical MRCI calculations. Additionally, a

diabatic natural orbital analysis revealed that the ionic and covalent characters of the  $\tilde{X}$  and  $\tilde{A}$  diabatic states were maintained as the Li-H bond is stretched, as should be the case for good diabatic states. For pyrazine, a model vibronic coupling Hamiltonian was constructed by direct fitting to DFT/MRCI P-BDD diabatic potentials. The model potential was subsequently used in MCTDH quantum dynamics simulations to compute the  $1B_{2u}(\pi\pi^*)$  state vibronic absorption spectrum. Almost quantitative agreement between the simulated and experimental spectra was attained, providing further validation of the accuracy of the DFT/MRCI P-BDD diabatic potentials.

We close by noting that the ability to rapidly and accurately determine diabatic potentials will be directly applicable to on-the-fly quantum dynamics simulations. In particular, the combination of DFT/MRCI P-BDD calculations and on-the-fly machine learning[50–54] holds promise for the construction of a powerful, near-black box framework for the use of DFT/MRCI in on-the-fly dynamics calculations, and will be the focus of future work in our group.

## VI. ACKNOWLEDGMENTS

We would like to thank Christel Marian and Martin Kleinschmidt for providing the original DFT/MRCI code that was modified for use in this work.

## Appendix A: Normal equations fitting of the model potentials

The fitting of the one- and two-mode terms in Equation 31,  $\tau_{p\alpha}^{(I,J)}$  and  $\eta_{\alpha\beta}^{(I,J)}$ , respectively, were fitted sequentially, starting with the one-mode terms.

### 1. Fitting of the one-mode terms

Let  $\mathbf{Q}_0^\alpha$  be the vector  $\mathbf{Q}_0$  with the  $\alpha$ th element removed, and  $W_{IJ}(Q_\alpha, \mathbf{Q}_0^\alpha)$  denote the value of the quasi-diabatic potential matrix element  $W_{IJ}$  displaced only along the single mode  $Q_\alpha$  at the geometry  $(0, \dots, 0, Q_\alpha, 0, \dots, 0)$ . Our model potential for displacements along a single mode  $Q_\alpha$  reads

$$W_{IJ}^{mod}(Q_\alpha, \mathbf{Q}_0^\alpha) = \tau_0^{(I,J)} + \sum_{p=1}^4 \frac{1}{p!} \tau_{p\alpha}^{(I,J)} Q_\alpha^p. \quad (\text{A1})$$

Let  $\{W_{IJ}(Q_\alpha, \mathbf{Q}_0^\alpha)_i : i = 1, \dots, n\}$  denote the set of ‘true’ quasi-diabatic potential matrix element values calculated at a number,  $n$ , of different geometries  $(Q_\alpha, \mathbf{Q}_0^\alpha)_i$  with only the mode  $Q_\alpha$  displaced. The squared one-mode residuals are defined as

$$\begin{aligned} |R_\alpha^{(I,J)}|^2 \equiv & \sum_{i=1}^n \left[ W_{IJ}(Q_\alpha, \mathbf{Q}_0^\alpha)_i - \tau_0^{(I,J)} \right. \\ & \left. - \sum_{p=1}^4 \frac{1}{p!} \tau_{p\alpha}^{(I,J)} (Q_\alpha^{(i)})^p \right]^2, \end{aligned} \quad (\text{A2})$$

where  $Q_\alpha^{(i)}$  is the value of  $Q_\alpha$  in  $(Q_\alpha, \mathbf{Q}_0^\alpha)_i$ . Requiring that the partial derivatives of the squared residual  $|R_\alpha^{(I,J)}|^2$  with respect to the parameters  $\tau_0^{(I,J)}$  and  $\tau_{p\alpha}^{(I,J)}$  vanish leads to the following system of linear equations:

$$\mathbf{X}_\alpha \mathbf{t}_\alpha^{(I,J)} = \mathbf{w}_\alpha^{(I,J)}, \quad (\text{A3})$$

with

$$\mathbf{X}_\alpha = \begin{pmatrix} 1 & Q_\alpha^{(1)} & \dots & (Q_\alpha^{(1)})^4 \\ 1 & Q_\alpha^{(2)} & \dots & (Q_\alpha^{(2)})^4 \\ \vdots & \vdots & \ddots & \vdots \\ 1 & Q_\alpha^{(n)} & \dots & (Q_\alpha^{(n)})^4 \end{pmatrix}, \quad (\text{A4})$$

$$\mathbf{t}_\alpha^{(I,J)} = \begin{pmatrix} \tau_0^{(I,J)} \\ \frac{1}{1!} \tau_{1\alpha}^{(I,J)} \\ \vdots \\ \frac{1}{4!} \tau_{4\alpha}^{(I,J)} \end{pmatrix}, \quad (\text{A5})$$

$$\mathbf{w}_\alpha^{(I,J)} = \begin{pmatrix} W_{IJ}(Q_\alpha, \mathbf{Q}_0^\alpha)_1 \\ W_{IJ}(Q_\alpha, \mathbf{Q}_0^\alpha)_2 \\ \vdots \\ W_{IJ}(Q_\alpha, \mathbf{Q}_0^\alpha)_n \end{pmatrix} \quad (\text{A6})$$

This yields the following solution for the optimal set of one-mode coefficients:

$$\mathbf{t}_\alpha^{(I,J)} = \left( \mathbf{X}_\alpha^T \mathbf{X}_\alpha \right)^{-1} \mathbf{X}_\alpha^T \mathbf{w}_\alpha^{(I,J)}. \quad (\text{A7})$$

In the fitting of the one-mode terms, for each mode  $Q_\alpha$  quasi-diabatic potential matrices  $\mathbf{W}(\mathbf{Q})$  were calculated at 21 geometries  $(Q_\alpha, \mathbf{Q}_0^\alpha)_i = (i\Delta Q_\alpha, \mathbf{Q}_0^\alpha)$ ,  $\Delta Q_\alpha = 0.5$ ,  $i = -10, \dots, 0, \dots, 10$ .

### 2. Fitting of the two-mode terms

Once the one-mode terms  $\tau_{p\alpha}^{(I,J)}$  have been determined, the two-mode terms  $\eta_{\alpha\beta}^{(I,J)}$  can be calculated from fitting to the values of the diabatic potential matrix elements  $W_{IJ}(\mathbf{Q})$  calculated at geometries  $\mathbf{Q} = (Q_\alpha, Q_\beta, \mathbf{Q}_0^{\alpha\beta})$  with two, and only two, modes displaced. Here,  $\mathbf{Q}_0^{\alpha\beta}$  denotes the vector  $\mathbf{Q}_0$  with the  $\alpha$ th and  $\beta$ th elements removed, and  $(Q_\alpha, Q_\beta, \mathbf{Q}_0^{\alpha\beta})$  is to be equated with the vector  $(0, \dots, 0, Q_\alpha, 0, \dots, 0, Q_\beta, 0, \dots, 0)$ . The part of  $W_{IJ}(\mathbf{Q})$  corresponding to the two-body correlation of the modes  $Q_\alpha$  and  $Q_\beta$ , denoted by  $\tilde{W}_{IJ}^{\alpha\beta}(Q_\alpha, Q_\beta)$ , can be obtained as

$$\begin{aligned} \tilde{W}_{IJ}^{\alpha\beta}(Q_\alpha, Q_\beta) = & W_{IJ}(Q_\alpha, Q_\beta, \mathbf{Q}_0^{\alpha\beta}) \\ & - W_{IJ}(\mathbf{Q}_0) - W_{IJ}(Q_\alpha, \mathbf{Q}_0^\alpha) - W_{IJ}(Q_\beta, \mathbf{Q}_0^\beta). \end{aligned} \quad (\text{A8})$$

In our model potential,  $\tilde{W}_{IJ}^{\alpha\beta}(Q_\alpha, Q_\beta)$  is approximated as

$$\tilde{W}_{IJ}^{\alpha\beta}(Q_\alpha, Q_\beta) \approx \eta_{\alpha\beta}^{(I,J)} Q_\alpha Q_\beta. \quad (\text{A9})$$

Thus, we minimise the following squared two-mode residuals with respect to the two-mode terms  $\eta_{\alpha\beta}^{(I,J)}$ :

$$\left| R_{\alpha\beta}^{(I,J)} \right|^2 \equiv \sum_{i=1}^n \left[ \tilde{W}_{IJ}^{\alpha\beta}(Q_\alpha, Q_\beta)_i - \eta_{\alpha\beta}^{(I,J)} Q_\alpha^{(i)} Q_\beta^{(i)} \right]^2, \quad (\text{A10})$$

where  $Q_\alpha^{(i)}$  and  $Q_\beta^{(i)}$  are the values of  $Q_\alpha$  and  $Q_\beta$  in the set of  $n$  geometries  $\{(Q_\alpha, Q_\beta, \mathbf{Q}_0^{\alpha\beta})_i\}$  at which the values  $\tilde{W}_{IJ}^{\alpha\beta}(Q_\alpha, Q_\beta)_i$  are calculated.

Minimisation of the squared residual  $|R_{\alpha\beta}^{(I,J)}|^2$  with respect to the parameter  $\eta_{\alpha\beta}^{(I,J)}$  yields the following equation:

$$\eta_{\alpha\beta}^{(I,J)} = \frac{\sum_{i=1}^n \tilde{W}_{IJ}^{\alpha\beta}(Q_\alpha, Q_\beta)_i}{\sum_{i=1}^n Q_\alpha^{(i)} Q_\beta^{(i)}} \quad (\text{A11})$$

Care must be taken here in the selection of the geometries  $(Q_\alpha, Q_\beta, \mathbf{Q}_0^{\alpha\beta})_i$  to be included in the fitting process as an improper selection will lead to the denominator in Equation A11 vanishing. Our choice corresponds to the diagonal cuts  $(Q_\alpha, Q_\beta, \mathbf{Q}_0^{\alpha\beta})_i = (i\Delta Q, i\Delta Q, \mathbf{Q}_0^{\alpha\beta})$ ,  $\Delta Q = 0.5$ ,  $i = -2, -1, 0, 1, 2$ .

Finally, we note that in our fitting scheme we approximate  $\tilde{W}_{IJ}^{\alpha\beta}(Q_\alpha, Q_\beta)$  using the prior fitted one-mode terms  $\tau_{p\alpha}^{(I,J)}$ :

$$\begin{aligned} \tilde{W}_{IJ}^{\alpha\beta}(Q_\alpha, Q_\beta) &\approx W_{IJ}(Q_\alpha, Q_\beta, \mathbf{Q}_0^{\alpha\beta}) \\ &- \tau_0^{(I,J)} - \sum_{p=1}^4 \left( \tau_{p\alpha}^{(I,J)} Q_\alpha^p + \tau_{p\beta}^{(I,J)} Q_\beta^p \right). \end{aligned} \quad (\text{A12})$$

For small displacements this will be a valid approximation.

### 3. Symmetry

It remains to note that many of the expansion coefficients  $\tau_{p\alpha}^{(I,J)}$  and  $\eta_{\alpha\beta}^{(I,J)}$  will be zero by symmetry. Specifically, the following relations hold:

$$\tau_{p\alpha}^{(I,J)} \neq 0, \quad \left\{ \bigotimes_{K=1}^p \Gamma^\alpha \right\} \otimes \Gamma^I \otimes \Gamma^J \ni \Gamma^1. \quad (\text{A13})$$

$$\eta_{\alpha\beta}^{(I,J)} \neq 0, \quad \Gamma^\alpha \otimes \Gamma^\beta \otimes \Gamma^I \otimes \Gamma^J \ni \Gamma^1, \quad (\text{A14})$$

where  $\Gamma^\alpha$  and  $\Gamma^I$  denote the irreducible representations generated by the mode  $Q_\alpha$  and the state  $\phi_I$ , respectively, and  $\Gamma^1$  the totally symmetric irreducible representation of the point group in question.

While it would be possible to omit from the fitting procedure those expansion coefficients that are zero by symmetry, we instead choose to include them and to monitor the fitted values of these. This allows for one to spot any possible symmetry breaking in the P-BDD calculations. A maximum value of  $3 \times 10^{-5}$  eV was attained for a coefficient that was zero by symmetry. All such parameters were omitted in the resulting MCTDH calculations, but this analysis does serve to demonstrate the symmetry-preserving properties of the P-BDD procedure.

- 
- [1] S. Grimme and M. Waletzke. *J. Chem. Phys.* **111**, 5645 (1999).
- [2] I. Lyskov, M. Kleinschmidt, and C. M. Marian. *J. Chem. Phys.* **144**, 034104 (2016).
- [3] A. Heil and C. M. Marian. *J. Chem. Phys.* **147**, 194104 (2017).
- [4] A. Heil, M. Kleinschmidt, and C. M. Marian. *J. Chem. Phys.* **149**, 164106 (2018).
- [5] N. Gavrilov, S. Salzmann, and C. M. Marian. *Chem. Phys.* **349**, 269 (2008).
- [6] S. Salzmann, M. Kleinschmidt, J. Tatchen, R. Weikauf, and C. M. Marian. *Phys. Chem. Chem. Phys.* **10**, 380 (2008).
- [7] C. M. Marian. *J. Chem. Phys.* **122**, 104314 (2005).
- [8] S. Perun, J. Tatchen, and C. M. Marian. *Chem. Phys. Chem.* **9**, 282 (2008).
- [9] S. P. Neville, O. M. Kirkby, N. Kaltsoyannis, G. A. Worth, and H. H. Fielding. *Nat. Commun.* **7**, 11357 (2016).
- [10] C. M. Marian, A. Heil, and M. Kleinschmidt. *Wiley Interdiscip. Rev. Comput. Mol. Sci.* **9**, 1394 (2019).
- [11] C. A. Mead and D. G. Truhlar. *J. Chem. Phys.* **77**, 6090 (1982).
- [12] G. J. Atchity and K. Ruedenberg. *Theor. Chem. Acc* **97**, 47 (1997).
- [13] H. Nakamura and D. G. Truhlar. *J. Chem. Phys.* **117**, 5576 (2002).
- [14] K. R. Yang, X. Xu, and D. G. Truhlar. *Chem. Phys. Lett.* **573**, 84 (2013).
- [15] H. Köppel. *Faraday Discuss.* **127**, 35 (2004).
- [16] H. Köppel. *Mol. Phys.* **104**, 1069 (2006).
- [17] T. Pacher, L. S. Cederbaum, and H. Köppel. *J. Chem. Phys.* p. 7367 (1988).
- [18] T. Pacher, L. S. Cederbaum, and H. Köppel. *Adv. Chem. Phys.* **84**, 293 (1993).
- [19] C. Robertson, J. González-Vázquez, I. Corral, S. Díaz-Tendero, and C. Díaz. *J. Comput. Chem.* **40**, 794 (2019).
- [20] G. W. Richings and G. A. Worth. *J. Phys. Chem. A* **119**, 12457 (2015).
- [21] C. E. Hoyer, X. Xu, D. Ma, L. Gagliardi, and D. G. Truhlar. *J. Chem. Phys.* **141**, 114104 (2014).
- [22] X. Zhu and D. R. Yarkony. *J. Chem. Phys.* **132**, 104101 (2010).
- [23] Y. Guan, H. Guo, and D. R. Yarkony. *J. Chem. Phys.* **150**, 214101 (2019).
- [24] T. Pacher, C. A. Mead, L. S. Cederbaum, and H. Köppel. *J. Chem. Phys.* **91**, 7057 (1989).
- [25] W. Domcke, C. Woywod, and M. Stengle. *Chem. Phys. Lett.* **226**, 257 (1994).
- [26] W. Domcke and C. Woywod. *Chem. Phys. Lett.* **216**, 362 (1993).
- [27] F. Venghaus and W. Eisfeld. *J. Chem. Phys.* **144**, 114110 (2016).
- [28] N. Wittenbank, F. Venghaus, D. Williams, and W. Eisfeld. *J. Chem. Phys.* **145**, 184108 (2016).
- [29] R. J. Cave and J. F. Stanton. *J. Chem. Phys.* **140**, 214112 (2014).
- [30] L. S. Cederbaum, J. Schirmer, and H. D. Meyer. *J. Phys. A* **22**, 2427 (1989).
- [31] F. Plasser, M. Ruckebauer, S. Mai, M. Oppel, P. Marquetand, and L. González. *J. Chem. Theory Comput.* **12**, 1207 (2016).
- [32] R. Kosloff and H. Tal-Ezer. *Chem. Phys. Lett* **127**, 223 (1986).
- [33] H. D. Meyer, U. Manthe, and L. S. Cederbaum. *Chem. Phys. Lett.* **165**, 73 (1990).
- [34] M. H. Beck, A. Jäckle, G. A. Worth, and H. D. Meyer. *Physics Reports* **324**, 1 (2000).
- [35] G. A. Worth, H.-D. Meyer, H. Köppel, L. S. Cederbaum, and I. Burghardt. *Int. Rev. Phys. Chem.* **27**, 569 (2008).
- [36] G. A. Worth, K. Giri, G. Richings, I. Burghardt, M. H. Beck, A. Jäckle, and H. D. Meyer, *The quantics package, version 1.1*, University of Birmingham, Birmingham, UK (2015) ().
- [37] J. C. Light, I. P. Hamilton, and J. V. Lill. *J. Chem. Phys.* **82**, 1400 (1985).
- [38] H. Köppel, W. Domcke, and L. S. Cederbaum. *Adv. Chem. Phys.* **57**, 59 (1984).
- [39] L. S. Cederbaum, H. Köppel, and W. Domcke. *Int. J. Quantum Chem.* **20**, 251 (1981).
- [40] *TURBOMOLE V6.1 2009, a development of University of Karlsruhe and Forschungszentrum Karlsruhe GmbH, 1989-2007, TURBOMOLE GmbH, since 2007; available from <http://www.turbomole.com>* ().
- [41] H. Lischka, R. Shepard, I. Shavitt, R. M. Pitzer, M. Dallos, T. Müller, P. G. Szalay, F. B. Brown, R. Ahlrichs, H. J. Bhm, A. Chang, D. C. Comeau, R. Gdanitz, H. Dachsel, C. Ehrhardt, M. Ernzerhof, P. Hchtl, S. Irle, G. Kedziora, T. Kovar, V. Parasuk, M. J. M. Pepper, P. Scharf, H. Schiffer, M. Schindler, M. Schler, M. Seth, E. A. Stahlberg, J.-G. Zhao, S. Yabushita, Z. Zhang, M. Barbatti, S. Matsika, M. Schuurman, D. R. Yarkony, S. R. Brozell, E. V. Beck, J.-P. Blaudeau, M. Ruckebauer, B. Sellner, F. Plasser, and J. J. Szymczak, *Columbus, an ab initio electronic structure program, release 7.0* ().
- [42] K. K. Innes, I. G. Ross, and W. R. Moomaw. *J. Mol. Spectrosc.* **132**, 492 (1988).
- [43] V. Engel. *Chem. Phys. Lett.* **189**, 76 (1992).
- [44] M. Stener, P. Decleva, D. M. P. Holland, and D. A. Shaw. *J. Phys. B: At. Mol. Opt. Phys.* **44**, 075203 (2011).
- [45] H. Keller-Rudek, G. K. Moortgat, R. Sander, and R. Sørensen. *Earth Syst. Sci. Data* **5**, 365 (2013).
- [46] L. Seidner, G. Stock, A. L. Sobolewski, and W. Domcke. *J. Chem. Phys.* **96**, 5298 (1992).
- [47] C. Woywod, W. Domcke, A. L. Sobolewski, and H.-J. Werner. *J. Chem. Phys.* **100**, 1400 (1994).
- [48] G. A. Worth, H. D. Meyer, and L. S. Cederbaum. *J. Chem. Phys.* **105**, 4412 (1996).
- [49] A. Raab, G. A. Worth, H. D. Meyer, and L. S. Cederbaum. *J. Chem. Phys.* **110**, 936 (1999).
- [50] G. W. Richings and S. Habershon. *Chem. Phys. Lett.* **683**, 228 (2017).
- [51] G. W. Richings and S. Habershon. *J. Chem. Theory Comput.* **13**, 4012 (2017).
- [52] G. W. Richings and S. Habershon. *J. Chem. Phys.* **148**, 134116 (2018).
- [53] G. W. Richings and S. Habershon. *J. Chem. Theory Comput.* **15**, 857 (2019).
- [54] I. Polyak, G. W. Richings, S. Habershon, and P. J. Knowles. *J. Chem. Phys.* **150**, 041101 (2019).